Characterizing Within-Die and Die-to-Die Delay Variations Introduced by Process Variations and SOI History Effect

Jim Aarestad, Charles Lamech, Jim Plusquellic
Univ. of New Mexico
Albuquerque, NM
jaarestad3@comcast.net, clamech, jimp@ece.unm.edu

Dhruva Acharyya
Verigy Inc.
Cupertino, CA
dhruva.acharyya@verigy.com

Kanak Agarwal
IBM, ARL
Austin, TX
kba@us.ibm.com

ABSTRACT

Variations in delay caused by within-die and die-to-die process variations and SOI history effect increase timing margins and reduce performance. In order to develop mitigation techniques to reduce the detrimental effects of delay variations, particularly those that occur within-die, new methods of measuring delay variations within actual products are needed. The data provided by such techniques can also be used for validating models, i.e., can assist with model-to-hardware correlation. In this paper, we propose a flush delay technique for measuring both regional delay variations and SOI history effect and validate the method using a test structure fabricated in a 65 nm SOI process.

Categories and Subject Descriptors

B.8.2[**Hardware**]:Performance and Reliability - Performance Analysis and Design Aids

General Terms

Experimentation

Keywords

Embedded Test Structure, Design for Manufacturability

1.INTRODUCTION

It is well established that the voltage on the isolated body of an SOI device varies as a function of its switching history and this voltage variation affects the threshold voltage of the device [1-5]. The variation in threshold voltage impacts the magnitude of the drain current and switching speed. Therefore, the switching speed of an SOI logic path depends on how often the path is exercised, with more frequent excitations resulting in faster switching speeds. The magnitudes of the delay variations vary widely (up to 15% per stage delay according to [1]) and depend on several process parameters, including well implantation, gate oxide thickness and halo implantation [4].

Previous works propose a variety of test structures for measuring delay variations introduced by SOI history effect (**HE**) [1][3] but many are fabricated and measured in dedicated, stand-alone test chip or scribe line contexts. In this paper, we propose a novel, minimally invasive technique that leverages the LSSD-style scan chain in actual products to allow HE-induced delay variations to be measured and analyzed.

Permission to make digital or hard copies of all or part of this work for personal or classroom use is granted without fee provided that copies are not made or distributed for profit or commercial advantage and that copies bear this notice and the full citation on the first page. To copy otherwise, to republish, to post on servers or to redistribute to lists, requires prior specific permission and/or a fee.
DAC'11, June 5-10, 2011, San Diego, California, USA
Copyright © 2011 ACM 978-1-4503-0636-2/11/06...$10.00

A similar strategy is proposed for measuring die-to-die and within-die delay variations. The global nature of the scan chain allows delay variations in different regions of the chip to measured. By configuring the scan chain into flush delay mode (which effectively turns it into a long delay chain) and using a timed sequence of launch/capture edges on the scan input and scan clocks, regional, within-die variations in delay can be captured as a digital thermometer code and scanned out for analysis.

Previous work on the characterization of within-die and die-to-die delay variations focus on the use of ring oscillators (RO) as the basic test structure [6-7], with the exception of [8], which uses a custom test structure based on a 64-bit Kogge-Stone adder. The authors report in [8] that within-die variation is spatially un-correlated but die-to-die variation is strongly correlated. In [9], the analysis of within-die and die-to-die delay variations show that die-to-die and layout-induced variations are significant.

Flush delay techniques have also been proposed, but in the context of fault detection [10], and speed-binning [11]. To our knowledge, this is the first time that flush delay is proposed and used for measuring and analyzing HE and regional delay variations.

The remainder of the paper is organized as follows. Section 2. describes the test structure used in the hardware experiments, as well as the proposed techniques. Section 3 presents a model for SOI history effect, whose behavior is validated in the experimental results presented in Section 4 using a set of 65 nm SOI test chips. We conclude in Section 5.

2.TEST STRUCTURE DESIGN AND EXPERIMENTAL TECHNIQUES

A block diagram of the test structure on the 65 nm chips is shown in Figure 1(a). The test-chip consists of an 80x50 array of test circuits (TCs) connected together through a scan chain. Each of the 4,000 TCs contains three master-slave FFs for a total of 12,000 FFs. The master-slave FFs are designed in an LSSD fashion, with separate clocks driving the master and slave latches as shown in Figure 1(b). The dual clock configuration allows a long delay chain to be created by setting both clocks high. Since each FF has two pass-gates and two inverters in series, the delay chain is effectively 48,000 gates long (12,000 FFs x 4 gates/FF).

2.1 SOI History Effect (HE)

For the SOI HE experiments, a series of five positive pulses are driven into the *scan in* pin as shown by the waveform labeled as 'Input Signal' in the top plot of Figure 2. With both A and B clocks high, the pulses propagate through the entire scan chain and emerge at the scan chain output as shown by the waveform labeled

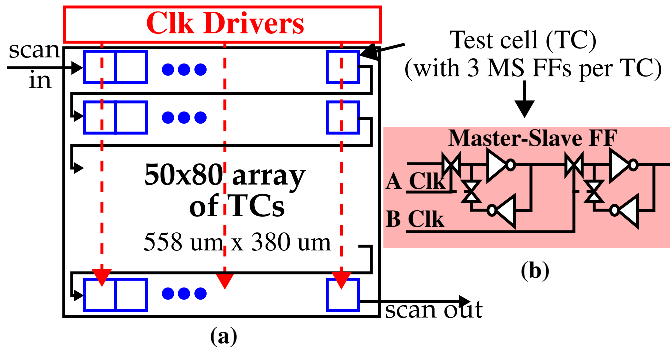

Figure 1. (a) Block diagram of test structure's scan path, and (b) FF with A/B Clocks to allow flush delay tests.

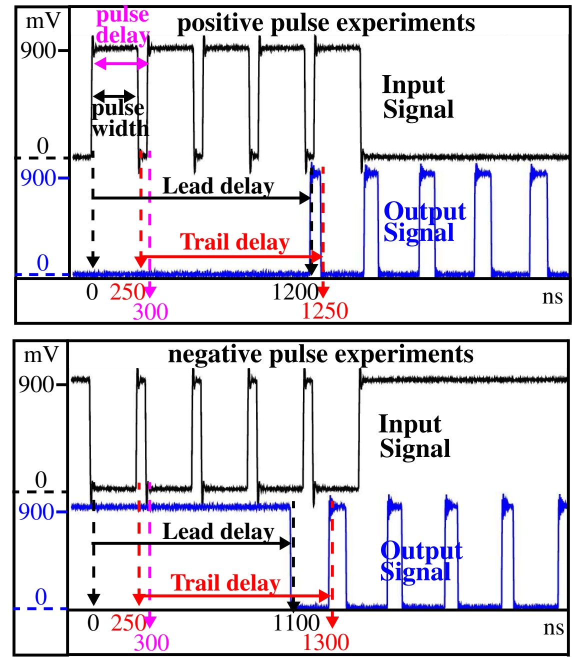

Figure 2. Example waveforms and timing characteristics for POS pulse (top) and NEG pulse (bottom) experiments.

as 'Output Signal' in Figure 2. The 'pulse delay' and 'pulse width' labels identify two additional parameters in our experiments. Pulse delay represents the time period between consecutive pulses, which varies over the range from 300 ns to 100,000 ns in 15 experiments. Three different pulse widths of 250 ns, 500 ns and 1000 ns are also investigated. The bottom plot in Figure 2 shows the input and output waveforms from a second set of negative pulse experiments.

The two timing parameters that we analyze are labeled as 'Lead delay' and 'Trail delay' in the plots of Figure 2. These delays are measured across the input and output waveforms between the rising and falling edges, respectively, as shown by the arrows in figure. It is clear from the figure that the width of the pulse that emerges from the scan chain changes across the five output pulses. These variations in pulse widths are caused HE. In particular, the width of the emerging positive and negative pulses grows larger for consecutive pulses in both experiments. The change in the width of the consecutive, emerging pulses reflects the charging/discharging time constants associated with the floating channels of the pass gates and inverters, and is explained by the model in the Section 3. The results presented in Section 4 demonstrate the rate and magnitude of change in the pulse widths is a function of the input pulse width and pulse delay (switching frequency).

2.2 Regional Delay

A similar setup is used for the regional delay experiments, i.e., the A and B clocks are held high. For these experiments, however, only a single rising edge is introduced into the scan chain input. In order to obtain the delay in different regions of the test structure, the A clock is used to stop the propagating edge at specific time intervals after the edge is launched into the scan chain input. For example, Figure 3 shows the scan in and A clock waveforms for the 50 ns experiment. A rising edge is launched at time 0 and the A clock is driven low 50 ns later. With the scan chain initialized to all 0s, the number of 1's captured in the scan chain indicates how far the edge propagated over the 50 ns time interval. Given the serpentine configuration of the scan chain as shown in Figure 1, longer timing delays between the launch/capture (**LC**) events measure the delay characteristics in larger portions of the array. We conducted a sequence of experiments on each of the chips in which the launch/capture delay was varied from 0 ns to approx. 1200 ns in 5 ns intervals, i.e., approx. 240 experiments were carried out per chip[1].

The number of FFs that the propagating edge traversed during any given 5 ns interval can be computed by subtracting the number of '1's measured under the previous test, e.g., the 45 ns LC test, from the number measured under the current test, e.g., the 50 ns

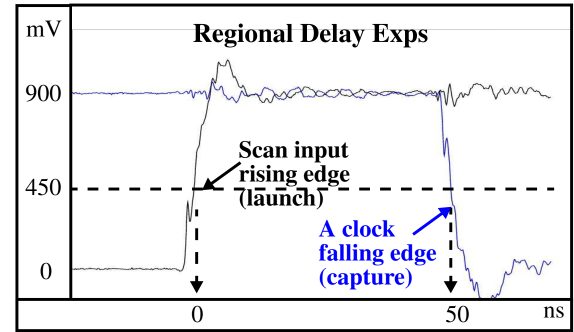

Figure 3. Waveforms from Regional Delay experiments showing launch/capture cycle for 50 ns experiment

LC test. In practice, measurement noise impacts the accuracy of the results but, fortunately, it can reduced by repeating the LC tests and computing an average. In our experiments, we repeated each experiment 12 times. Equation 1 gives the expression for computing the average number of additional FFs (*AFF*) traversed between any two tests, *k* and *k-n*. *N1* indicates the number of '1's read from

$$AFF_k = \frac{1}{12}\sum_{i=1}^{12}(N1_i - AFF_{k-n}) \qquad \textbf{Eq.1.}$$

the scan chain. This expression allows regional variations in delay to be analyzed at various levels of granularity by choosing appropriate values for *n*. The average delay per FF in each region can also be derived by dividing the difference in the LC time intervals of two tests *k* and *k-n* (each of which is a multiple of 5 ns) by the value obtained from Eq. 1.

1. The actual delay along the chain in each chip determined the number of experiments, which varied because of process variations.

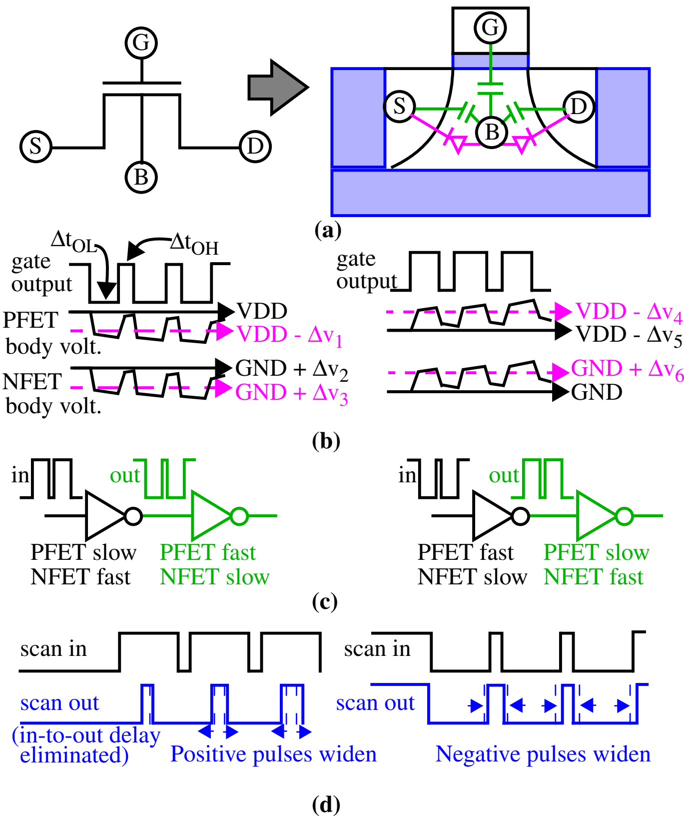

Figure 4. (a) Dominant sources of charge transfer in floating body of an SOI device, (b) est. of body potential swings for a switching inverter, and (c)(d) impact on inverter delays.

3.SOI HISTORY EFFECT (HE) MODELING

Figure 4(a) shows the dominant charge transfer paths to and from the floating body of an SOI NFET device. The body is capacitively coupled to the FET terminals and hence a switching event at the drain, source, or gate of the device can dynamically inject charge in and out of the body. The floating body can also lose or gain charge due to static leakages associated with the PN junction diodes formed between the body and the source/drain nodes, and gate leakage currents. The dynamic capacitive coupling effect and the static leakage mechanism combine to create the HE, which manifests itself in the form of delay dependence on the switching history.

Since we cannot observe the actual body voltage swings in our experiments, the analysis presented here is deduced from the observed behavior presented in the next section. We refer the reader to references [1-5] for details on the various parameters that impact body voltage behavior.

Figure 4(b) shows two scenarios for the NFET and PFET body voltage initial values and swings for an inverter configuration. The scenario on the left depicts the situation where the gate input remains at logic 0 for a long period before the rising transition occurs while the scenario on the right shows the opposite situation. Note the initial values of the body voltages of the NFETs and PFETs are indicated by the solid lines in both scenarios. With the gate at DC for a long period of time, the leakage mechanisms in the NFET and PFET define the magnitudes of these long-term DC body voltages. From simulations, these long-term DC values are below (above) VDD (GND) by approx. 25% of the supply rail range for PFETs (NFETs).

Consider the arrival of a rising transition on the input of the inverter in the left scenario. The rising input injects charge into the body of both devices due to gate-to-body coupling (Figure 4(a)). A rising input also results in a falling transition at the drain nodes which pulls the body potential lower (in both devices) due to drain-to-body capacitive coupling. The drain-to-body coupling effect dominates the gate coupling effect, which is easily justified considering the device is conducting. Following the rising input transition, the output of the inverter is low for a time period Δt_{OL} as shown in the figure. During this period, the leakage mechanisms work to move the body voltages toward their long-term DC values under the new output state. When the falling transition arrives on the gate input, the opposite occurs, i.e., both body voltage rise due to the coupling effect and subsequently, leakage works to pull them to the alternate long-term DC values. Note that the relative magnitudes of the coupling and leakage voltage variations shown in the figure depict one scenario of several that are possible.

The scenarios shown in Figure 4(b) purposely depict the duty cycles of the positive pulses on the inverter input as unequal. In particular, the duty cycle is greater than 50% for the scenario on the left, i.e., $\Delta t_{OL} > \Delta t_{OH}$, while it is less than 50% for the scenario on the right. The overall effect of the asymmetry in the duty cycle works to exacerbate the rate and magnitude of the “drift” of the body voltages to specific ‘average’ DC values (shown by the dotted lines). The average DC values occur between the maximums defined for the two long-term DC values. From the diagram, it is also apparent that the final ‘average’ body voltages are not attained instantaneously, but rather it takes a several cycles to reach them.

The variations in the average body voltages affect the threshold voltages of the PFET and NFET devices in each inverter, and the corresponding delay. Figure 4(c) labels the impact on the transistors in a two inverter chain, for each of the two scenarios shown in Figure 4(b). The downward movement of the body voltages for the scenario on the left degrades the responsiveness of the PFET in the first inverter increasingly over time, i.e., as more transitions occur on its input. At the same time, the responsiveness of the NFET improves. The overall effect on the inverter’s delay is that falling output transitions occur sooner in time than they would under the initial condition of the NFET body voltage, while rising output transitions occur later in time. Unfortunately, these variations in delay culminate at gates downstream as shown for the second inverter in the left scenario of Figure 4(c). Here, the opposite conditions exist, resulting in body voltage behavior as depicted in the right scenario of Figure 4(b).

Figure 4(d) shows the HE effect on the delay of a chain of inverters (a path) under each of the scenarios. The stimulus applied to the path input is labeled as ‘scan in’ (to relate it to our test structure shown in Figure 1), while the response waveform on the path output is labeled ‘scan out’. The ‘scan out’ waveform has been skewed to the left in time, i.e., the overall path delay is eliminated, to allow comparisons of pulse widths between the input and output waveforms. Differences in the capacitive loads along the path and HE both act to change width of the output pulses in both scenarios (also shown in Figure 2). However, delays introduced by HE additionally change over time, which is reflected across the sequence of output pulse widths. In both scenarios, consecutive pulses become increasing wider (dotted lines show the expected result without HE) because the first edge is sped up while the second edge is slowed down.

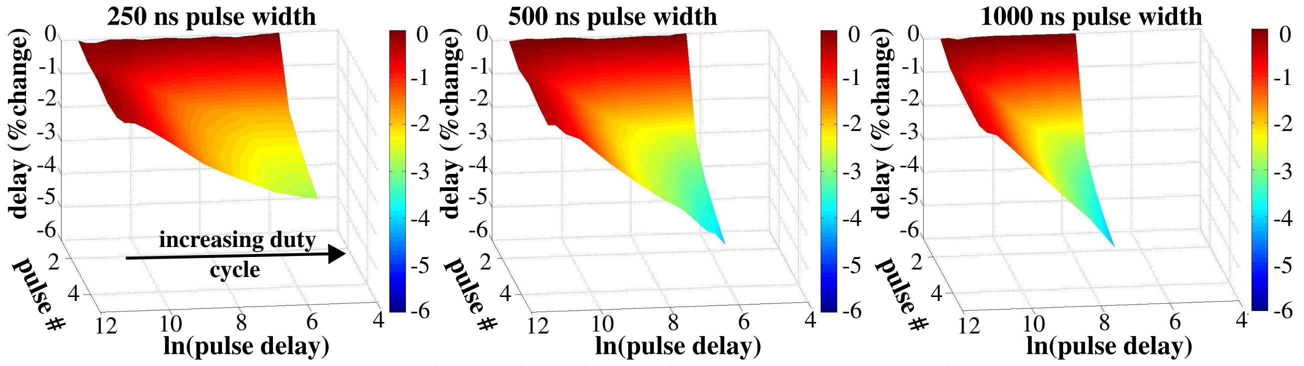

Figure 5. Percentage change in delay of the LEADING edge of a positive pulse emerging from the scan chain output plotted against ln(pulse delay) (x-axis) and pulse number (y-axis) showing SOI history effect.

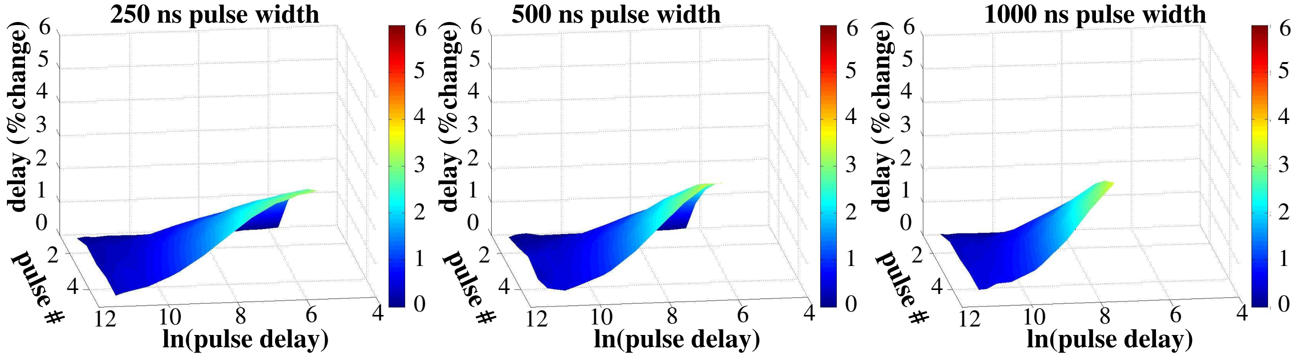

Figure 6. Percentage change in delay of the TRAILING edge of a positive pulse emerging from the scan chain output plotted against ln(pulse delay) (x-axis) and pulse number (y-axis) showing SOI history effect.

4.EXPERIMENTAL RESULTS

4.1 SOI History Effect

The experiments described in Section 2. allow delay variations introduced by HE to be measured as a function of several parameters. As indicated in the previous section, the main contributor to delay variation introduced by HE is the frequency of excitation of the logic path. A second contributor is the relative amount of time the logic path is maintained in one of the two possible states. To investigate these parameters, we apply a set of five pulses to the *scan in* input as shown in Figure 1 using a variety of *pulse delay* and *pulse width* values. Most of the previous work focuses on 'first-switch, second-switch'. In this work, we show that HE plays a role in delay variations beyond the second switch, and the variation in delay over the sequence of pulses behaves like a RC time constant.

As an illustration of the impact of HE on delay, Figures 5 and 6 show the results obtained from a sequence of positive pulse experiments carried out on one of our chips. In each 3D plot, the x-axis plots the *ln* (natural log) of the pulse delay in ns, with range of 4 to 12 from right to left. The actual pulse delays used were 300, 400, 500, 600, 800, 1,000, 2,000, 4,000, 8,000, 16,000, 20,000, 40,000, 60,000, 80,000 and 100,000 ns. The y-axis represents the pulse number from 5 (front) to 1 (back) while the z-axis plots the percentage change in delay under each of these 75 experiments (15 * 5). The percentage change (*pch*) is computed with respect to the upper left-most data point, i.e., the *reference* delay is the delay of the first pulse under pulse delay experiment of 100,000 ns. Eq. 2 gives the expression for *pch* where d_t represents the measured delay in experiment *t* (measured as shown in Figure 2) and d_{ref} is the reference delay. Each of the three plots in Figure 5 show the

$$\text{pch} = \frac{(d_t - d_{\text{ref}})}{d_{\text{ref}}} 100 \qquad \textbf{Eq.2.}$$

delays of the leading edge in experiments with the pulse width set to 250 ns, 500 ns or 1,000 ns (note, the smaller values of pulse delays, e.g., 300 ns, are not relevant for the 500 ns and 1000 ns pulse width experiments). Figure 6 gives the results for the trailing edge under the same conditions.

The negative values on the z-axis from Figure 5 indicate that the reference experiment generates the longest leading edge delay For the 100,000 ns pulse delay experiment, the long Δt between each pulse allows the long-term DC body voltage conditions to be re-established. Therefore, the leading edge delays portrayed on the left side of the surface plots are constant and nearly equal to the reference delay. As the frequency of the pulses is increased, the delay of the first edge remains constant (back edge of plots). However, subsequent pulses begin to experience HE, resulting in a smaller delay of approx. 4-5% for this chip. HE takes hold earlier and more significantly for wider, i.e. 500 ns and 1,000 ns, pulse widths, as shown by the center and right-most plots. The trailing edge analysis shown in Figure 6 depicts opposite behavior, where the delays of the trailing edges from later pulses under higher pulse frequencies increase.

In order to add perspective with regard to the magnitude of delay variation introduced by HE, we compare it with chip-to-chip process variations in Figure 7. The graph plots the delays of the 1st and 5th leading and trailing edges obtained from the set of 500 ns pulse width, 600 ns pulse delay experiments along the y-axis for each of our 35 chips (x-axis). The chips are sorted by the delays measured under the positive pulse, leading edge experiments (top-

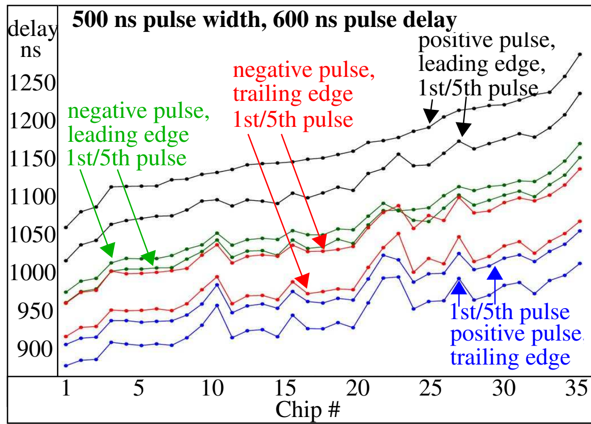

Figure 7. Delay variation between 1st and 5th pulses (y-axis) for 35 chips (x-axis) in positive and negative pulse exps.

most waveform). Each of the four pairs of waveforms corresponds to the delays of one of the edges (leading or trailing) in either the positive and negative pulse experiments.

Given this plot, it is straightforward to compute the relative variations introduced by global process variations and HE. The % change in delay, measured using the left-most and right-most data points in the top-most waveform is approx. 21%, while the % change due to HE is approx. 4.5%, given by the left-most data points of the top two waveforms. The % change in the negative pulse, trailing edge waveforms is similar but opposite in polarity, and is smaller for the other two waveform pairings. Interestingly, HE delay variations are relatively constant across the chips, i.e., the vertical spacing between waveform pairs, and therefore appear to be relatively insensitive to process variations.

A third interesting observation is the difference in the vertical spacings of the waveform pairs associated with the positive and negative pulse experiments. The positive pulse waveforms occupy the vertical extremes, which is counter-intuitive given the symmetry of a scan chain architecture. However, our scan chain is not completely symmetrical as illustrated in Figure 1. In particular, the right-most TCs on each row drive long wires that connect the last element of the row with the first element of the next row. As indicated in Section 2, each row has an even number of FFs (and inverters). Therefore, the positive pulse experiment requires the inverters on the right edge of the array to drive a rising edge onto each of these long wires (80 total). Given that PFETs tend to be weaker drivers than NFETs, this contributes to the asymmetrical offsets associated with the waveform pairs in Figure 7. A second, more important, asymmetry that exists in the chain is the difference in the capacitive loads driven by the outputs of the FFs (not shown). In particular, the slave components of the FFs drive an additional fanout load (in addition to the input of the next FF). These asymmetries add approx. 8% variation in delay. However, unlike HE and process variations, this source of variation can be eliminated by sizing the transistors appropriately.

4.2 Regional Delay Variations

Using the launch/capture scheme described in Section 2.2, we were also able to measure regional delay variations, and compare them with the chip-to-chip variations reported in the previous section. As described in Section 2.2, we carried out a sequence of experiments on each chip in which the capture event (the act of driving the A clock low) was increased from 0 ns to approx. 1200 ns in 5 ns increments. After each launch/capture experiment, both

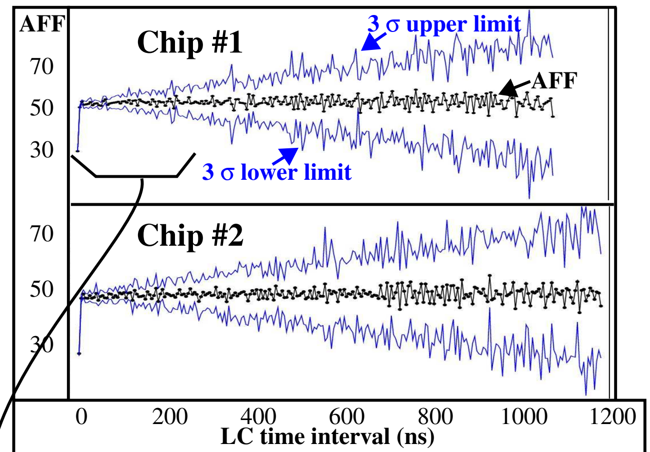

Figure 8. Regional delay experiments showing average number of FFs (AFF) traversed during each 5 ns time interval.

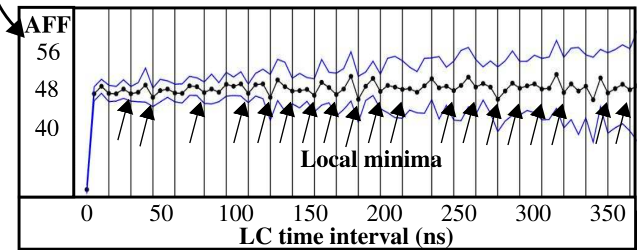

Figure 9. Blow-up of Chip #2 regional delay experiments.

the A and B clocks were used to scan out the sequence of 12,000 bits to determine how far the propagating edge advanced through the scan chain.

Figure 8 shows the results for two of our chips. The x-axis gives the LC time interval while the y-axis plots the average number of FFs (AFF) traversed during each consecutive 5 ns time interval, computed using Equation 1. The center waveform represents the AFF values while the bounding waveforms (top and bottom) represent the upper and lower 3 σ limits (computed using the 12 samples taken for each LC test). The AFF values vary around 52 and 48 for Chip #1 and #2, resp. which indicates the number of FFs that the edge propagates through during each 5 ns time interval. The limits increase from left to right for both chips, indicating that the level of uncertainty increases for regions at the bottom of the array (see Figure 1).

A blow-up of the left-most region of Chip #1 from Figure 8 is shown in Figure 9. The vertical bars in the plot identify time intervals in which the propagating edge moves onto a new row in the array. The long wires connecting consecutive rows add wire delay and should therefore reduce the AFFs traversed in these LC tests. The arrows shown in Figure 9 illustrate where local minima occur in the measured AFF values. The absence of some local minima illustrates that although the wire delay component is measurable, the uncertainty in the measurements makes it difficult to measure them accurately. This is particularly evident in lower regions of the array (not shown in Figure 9) where the level of uncertainty increases.

Although the analysis of regional delay variations at the 5 ns scale is interesting, it is dominated by local (and random) process variation effects. The large magnitude of these random variations make it difficult to observe within-die and across-macro systematic delay variations. As indicated in Section 2.2, the parameters to

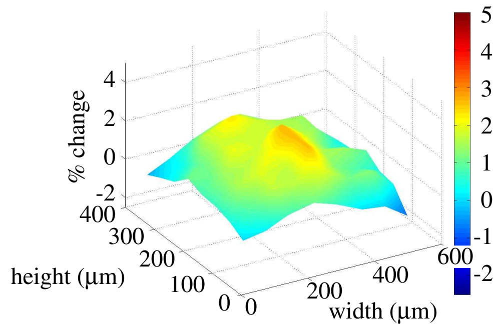

Figure 10. Regional I_{on} variations across the array.

Equation 1 allow other levels of granularity of delay variations to be measured and analyzed.

In particular, we are interested in determining if the variation in I_{on} current, as shown in Figure 10, is correlated to regional delay variations. The (x,y) plane of the figure represents the spatial domain of the array while the z-axis plots the percentage change in the magnitude of I_{on} currents in different regions of the array. From the figure, it is clear that I_{on} is larger in the central region of the array, and decreases toward the edges.

Systematic, within-die variations in delay are more easily observed by partitioning the array shown in Figure 1 into larger regions. We use Equation 1 to derive regional delay variations at granularities of 8 and 16 by dividing the total number of LC tests by these numbers and computing a 'normalized' AFF value for each segment. This is accomplished by computing the AFF value for each segment (using Equation 1) and dividing by the number of LC tests in each segment. Intuitively, the larger regions also reduce the level of uncertainty in the reported values.

Figure 11(a) and (b) give the results for the 8 and 16 segment analyses, respectively, for 36 chips. The segments are plotted along the x-axis (in reverse order), chip numbers along the y-axis, and the normalized, regional delays as percentage change along the z-axis. The reference component is segment #1 from chip #1 (lower, right-most element). Although die-to-die variations are clearly visible, the within-die delay variations are also observable. In particular, the values on the edges of the graphs, i.e., those corresponding to segments 1 and 8 from Figure 11(a) and to 1 and 16 from Figure 11(b), are slightly smaller for each chip by approx. 1-2% under the 8 segment analysis, and 2-3% for the 16 segment analysis. This correlates well with the I_{on} analysis presented in Figure 10, that shows about a 5% reduction along the edges when compared with the central portion of the array. Given the regions analyzed under the delay analysis are 1-D in nature (in the y dimension of the array only), we expect only the top (segment 1) and bottom (segment 8 or 16) components to be smaller than the other regions. This is true because increases in delay for gates along the left and right edge of the array appear in every segment and therefore cancel out. This, in turn, reduces the magnitude of the measured delay variations to about half of that measured for I_{on}.

5.Conclusions

In this paper, we proposed two FLUSH delay based techniques for measuring delay variations introduced by SOI history effect and regional process variations. The analysis was carried out on a test structure fabricated in IBM's 65 nm SOI technology. The

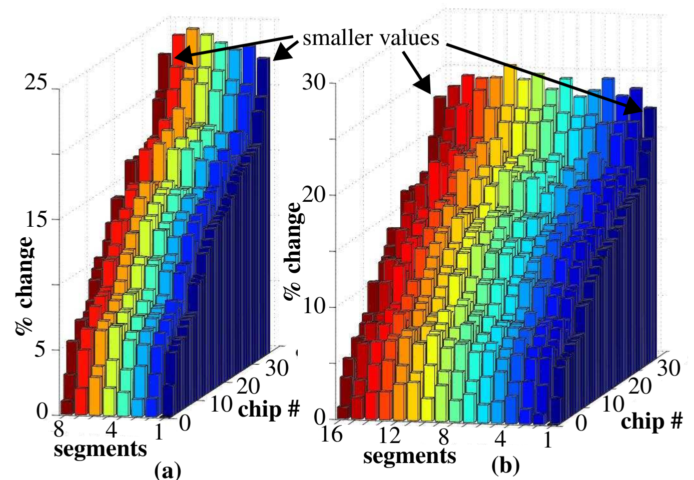

Figure 11. Regional delay variations across 10 chips (y-axis) with the array partitioned into (a) 8 regions, (b) 16 regions.

results show that worst case delay variations introduced by HE are approx. 4.5% while those caused by chip-to-chip process variations can be as large as 21%. Worst case systematic, within-die process variations introduce delay variations of approx. 1-3% while those caused by random, within-die process variations can be as large as 10%.

6.ACKNOWLEDGEMENTS

We thank Jerry Hayes and Sani Nassif of Austin Research Laboratory for their support of this research.

7.REFERENCES

[1]K. A. Jenkins, S. Kim, S. P. Kowalczyk, D. Friedman, "Impact of SOI History Effect on Random Data Signals," in Proc. of *Integrated Circuit Design and Technology*, 2007, pp. 1-4.

[2]S. Narendra, J. Tschanz, A. Keshavarzi, S. Borkar, V. De, "Comparative Performance, Leakage Power and Switching Power of Circuits in 150 nm PD-SOI and Bulk Technologies including Impact of SOI History Effect," in Proc. *VLSI Circuits*, 2001, pp. 217-218.

[3]O. Faynot, T. Poiroux, J. Cluzel, M. Belleville, J. de Pontcharra, "A New Structure for In-Depth History Effect Characterization on Partially Depleted SOI Transistors," in Proc. of *SOI Conference*, 2002, pp. 35-36.

[4]Q. Liang *et al*, "Optimizing History Effects in 65nm PD-SOI CMOS," in Proc. of *SOI Conference*, 2006, pp. 95-96.

[5]S.K.H. Fung *et al*, "Controlling floating-body effects for 0.13 um and 0.10 um SOI CMOS", In Proc. of Electron Devices Meeting, 2000, pp. 231

[6]B.P. Das, B. Amrutur, H.S. Jamadagni, N.V. Arvind, V. Visvanathan, "Within-Die Gate Delay Variability Measurement using Re-configurable Ring Oscillator," in Proc. of *Custom Integrated Circuits Conference*, 2008, pp. 133-136.

[7]H. Onodera, H. Terada, "Characterization of WID Delay Variability using RO-array Test Structures," in Proc. of *International Conference on ASIC*, 2009, pp. 658-661.

[8]N. Drego, A. Chandrakasan, D. Boning, "All-Digital Circuits for Measurement of Spatial Variation in Digital Circuits," *Solid-State Circuits*, vol.45, no.3, 2010, pp. 640-651.

[9]P. Liang-Teck, B. Nikolic, "Measurements and Analysis of Process Variability in 90 CMOS," *Solid-State Circuits*, vol.44, no.5, May 2009, pp. 1655-1663.

[10]F. Yang, S. Chakravarty, N. Devta-Prasanna, S.M. Reddy, I. Pomeranz, "On the Detectability of Scan Chain Internal Faults An Industrial Case Study," in Proc. of *VLSI Test Symposium*, 2008, pp. 79-84.

[11]C. Thibeault, "On the Potential of Flush Delay for Characterization and Test Optimization," in Proc. of *Current and Defect Based Testing Workshop*, 2004, pp. 55- 60.